Bohm, M., Haberland, C., Asch, G. (2013): Imaging fluid-related subduction processes beneath Central Java (Indonesia) using seismic attenuation tomography. - Tectonophysics, 590, 175-188

DOI: 10.1016/j.tecto.2013.01.021

Imaging fluid related subduction processes beneath Central Java (Indonesia) using seismic attenuation tomography

Mirjam Bohm [a], Christian Haberland [a,*], Günter Asch [a],

[a] *Helmholtzzentrum Potsdam Deutsches GeoForschungsZentrum, Germany*

Abstract

We use local earthquake data observed by the amphibious, temporary seismic MERAMEX array to derive spatial variations of seismic attenuation (Q_p) in the crust and upper mantle beneath Central Java. The path-averaged attenuation values (t^*) of a high quality subset of 84 local earthquakes were calculated by a spectral inversion technique. These 1,929 t^*-values inverted by a least-squares tomographic inversion yield the 3D distribution of the specific attenuation (Q_p). Analysis of the model resolution matrix and synthetic recovery tests were used to investigate the confidence of the Q_p-model. We notice a prominent zone of increased attenuation beneath and north of the modern volcanic arc at depths down to 15 km. Most of this anomaly seems to be related to the Eocene-Miocene Kendeng Basin (mainly in the eastern part of the study area). Enhanced attenuation is also found in the upper crust in the direct vicinity of recent volcanoes pointing towards zones of partial melts, presence of fluids and increased temperatures in the middle to upper crust. The middle and lower crust seems not to be associated with strong heating and the presence of melts throughout the arc. Enhanced attenuation above the subducting slab beneath the marine forearc seems to be due to the presence of fluids.

Key words: attenuation tomography, Central Java, Sunda Arc, subduction, crust and upper mantle structure

1 Introduction

Fluids are considered to play an important role in all processes occurring in subduction zones (e.g., Peacock, 1990; Saffer and Tobin, 2011). In the frontal forearc water is dispelled from down-dragged sea floor sediments. Metamorphic reactions of the sediments and within the subducting crust and mantle provide additional aqueous fluids (e.g., Ranero et al., 2003). The input of these fluids into the mantle tip results in serpentinization of the mantle material thus controlling the downdip limit of great subduction thrust earthquakes (Hyndman and Peacock, 2003). Moreover, the fluid pressure distribution along the subduction interface seems to be related to different frictional domains along the megathrust (e.g., Saffer and Tobin, 2011, and references therein).

At greater depth it is assumed that the intermediate depth seismicity indicates dehydraton processes in the downgoing plate (e.g., Kirby et al., 1996), and that the input of these fluids into the asthenospheric mantle wedge triggers the generation of magmas at depth of around 125 km which eventually result in the subduction related volcanism (e.g., Gill, 1981; Tatsumi, 1989; Davies and Stevenson, 1992).

In this paper we study these fluid-related processes in Central/East Java (In-

* Corresponding author. GFZ Potsdam, Telegrafenberg, 14473 Potsdam, Germany, Tel.: +49-331-2881810, Fax: +49-331-288
Email address: haber@gfz-potsdam.de (Christian Haberland).

donesia) by analyzing the three-dimensional (3D) distribution of seismic attenuation (Q_p). The island forms part of the Sunda Arc in South-East Asia which stretches for more than 6,000 km from Timor to the Andaman Islands. The aim of the study is to gain an improved insight into these presumably coupled fluid-related processes and to derive constraints through comparison with similar studies in other regions and analysis of the specific conditions at this location.

The parameter of seismic attenuation ($1/Q_p$) - complementing the P-wave velocity and Poisson ratio - is known to be particularly sensitive to fluid content and high temperatures. Seismic attenuation is the loss of energy of a seismic wave when passing through rock (e.g., Aki and Richards, 1980), and it can be caused by a variety of mechanisms, most importantly by friction, fluid flow, viscous relaxation and scattering (e.g., Johnston et al., 1979). While intrinsic attenuation of minerals is generally small, frictional sliding between grains and across thin cracks is an important mechanism in porous media. Frictional sliding depends strongly on the saturation of the rocks with fluids, the properties of these fluids and the strength of the individual components of the matrix (e.g., Winkler and Murphy, 1995; Johnston et al., 1979). Another important mechanism of attenuation is viscosity and (macroscopic or local) flow of saturating fluids (Johnston et al., 1979). This is certainly an important mechanism in the crust where almost all rocks are partially or completely saturated with fluids, but also in zones of partial melt (Mavko, 1980; Mavko and Nur, 1975). At greater depth temperature seems to play the dominating role for attenuation through grain boundary relaxation and grain boundary sliding. In the mantle attenuation should be dominated by these thermally activated processes (Karato and Spetzler, 1990; Jackson et al., 2002; Sato et al.,

1989). For most dry rocks $Q_p/Q_s < 1$, while for saturated rocks $Q_p/Q_s \sim 1$ at surface pressure (Johnston et al., 1979). Finally, scattering also contributes to attenuation (e.g., Hoshiba et al., 2001).

The sensitivity of seismic attenuation regarding temperature and the presence of fluids (melts and water) makes it an ideal parameter to study the processes in subduction zones. Previous studies have revealed the attenuating structure in these zones around the world (Barazangi and Isacks, 1971; Barazangi et al., 1975; Sacks and Okada, 1974; Whitman et al., 1992; Chinn et al., 1980). The most detailed images are from local earthquake tomographic studies, imaging both the mantle and the crust (e.g., Hashida, 1989; Satake and Hashida, 1989; Roth et al., 1999; Tsumura et al., 2000; Haberland and Rietbrock, 2001; Eberhart-Phillips and Chadwick, 2002; Schurr et al., 2003; Stachnik et al., 2004; Eberhart-Phillips et al., 2008; Monna and Dahm, 2009; Chen and Clayton, 2009; Pozgay et al., 2009; Piccinini et al., 2010). At the same time, attenuation tomography has been succcessfully applied to volcanic and geothermal regions (e.g., Clawson et al., 1989; Ponko and Sanders, 1994; Wu and Lees, 1996; Romero et al., 1997).

We analyze local earthquake data observed by a large, temporary, amphibious, seismic network which was deployed in eastern Central Java for a period of about 150 days in 2004.

2 Geological setting

The island of Java is part of the Sunda Arc. Here, at the southwestern edge of the Eurasian continent, the Australian plate subducts beneath Sundaland

(e.g., Van Bemmelen, 1949, Figure 1). Related to this convergence, ophiolites, continental fragments (terranes) and volcanic arc material stranded at the Sundaland margin since the Cretaceous, were amalgamated, and form today most of the basement beneath Java (Simandjuntak and Barber, 1996; Smyth et al., 2007). From the middle Eocene (ca. 45 Myr) to the middle Miocene (ca. 20 Myr), a volcanic arc (Southern Mountains Arc, SMA) formed in the southern coastal region of the island (e.g., Smyth et al., 2008). North of the SMA, a large basin formed on the Sundaland shelf edge which is today preserved in Eastern Java in the Kendeng Zone.

After cessation of subduction in the Cretaceous, subduction resumed in the Late Miocene, and the modern volcanic arc developed approximately 50 km north of the SMA in the center of Java (Clements et al., 2009). Most of the Sunda Arc volcanoes are stratovolcanoes. Prominent active volcanoes of the Sunda Arc in Central and East Java, which are located roughly 100 km above the subducting slab, are Mt. Merapi, Mt. Merbabu, Mt. Telomoyo, Mt. Ungaran (all in the central part), Mt. Lawu (in the East), Mt. Sumbing, Mt. Sundoro, and the Dieng volcanic complex (in the western part of the study area). The high-K alkaline volcanoes Mt. Muria and Mt. Lassem are located in the backarc region(Edwards et al., 1991; Leterrier et al., 1990).

Java can be divided into three segments, West Java, Central Java and East Java, each having its own geological character. It has been proposed that the most fundamental structural division is between Central and East Java. This division is formed by the Muria-Progo lineament, a NNE-SSE lineament approximately at 110.5E, which links many features such as a structural high in the Java forearc, centres of Oligo-Miocene volcanoes (West Progo Volcanic complex), and the modern volcanoes of Mt. Merapi and Mt. Muria. This

lineament was first defined in Smyth et al. (2005). Moreover, a change from subduction accretion to subduction erosion has been observed at the transition between Central Java and Eastern Java (e.g., Kopp, 2011). The almost orthogonal convergence between the Australian plate and Eurasia is 67±7mm/yr today, providing the framework for intense subduction zone seismicity including mega-thrust earthquakes with high tsunami potential (e.g., Ammon et al., 2006). However, the study area is located in a region with relatively little seismicity. It had been suggested that the subduction of a prominent bathymetric feature, the Roo Rise, is responsible for the reduced seismicity (e.g. Newcomb and McCann, 1987).

3 Crustal structure from previous geophysical studies

Part of the dataset used in this study (see below) was analyzed to derive the crustal structure of Central Java. Koulakov et al. (2007) employed seismic travel time inversion (v_p and v_p/v_s) of the local earthquake dataset. Wagner et al. (2007) complemented the local earthquake data with controlled source data of an offshore experiment and jointly inverted this merged data set. Koulakov et al. (2009) extended the local earthquake tomographic inversion to include anisotropy.

These studies clearly show the inclined Wadati Benioff zone down to a depth of 150 km (the deepest earthquakes during the observation period occurred just north of Java at a depth of almost 300 km). A large number of earthquakes is found offshore at depths between 30 and 50 km. These events are diffusely collocated in an inclined plane and are most likely located at the plate interface as well as within the forearc (hanging wall). Some earthquakes are also found

in mid-crustal levels beneath Java. Intermediate depth seismicity is found between 50 and 150 km depth, forming a double seismic zone at depth between 80 and 150 km (Koulakov et al., 2007).

The velocity models are consistent with a crustal thickness of 30 to 40 km beneath Java. The marine forearc is characterized by rather high seismic v_p velocities in line with a thin offshore forearc crust and a shallow hydrated mantle (also derived by marine refraction seismics; see Kopp, 2011). The frontal forearc tip shows reduced seismic velocities consistent with the accretionary wedge. The most prominent feature in the velocity models is a strong anomaly of reduced velocities in the crust (30% in v_p, 36% in v_s), just north of the volcanic arc (Koulakov et al., 2007) which had been attributed to a high content of fluids and melts within the crust. Koulakov et al. (2009) note anisotropic conditions with differently oriented symmetries interpreted to be due to the regional stress regime and layering of sediments or lenses of partial melt, respectively. Further anomalies had been attributed to ascent paths of fluids and melts from deeper levels (Koulakov et al., 2007, 2009). Wagner et al. (2007) point out that the upper-crustal low-velocity anomaly is best expressed in the eastern/central part of the study area and relate it - partly - to "(...) lava and sedimentary deposits of the Kendeng Basin". Moreover, the Kendeng Basin is further characterized by a strong negative Bouguer gravity anomaly exceeding -58mGal suggesting that there are as much as 10 km of sediments at its thickest parts (Waltham et al., 2008; Untung and Sato, 1978). Magnetotelluric studies revealed two highly conductive zones north of the modern volcanic arc (Hoffmann-Rothe et al., 2001). Finally, a large number of geophysical studies target shallow structure and the volcanic activity of Mt. Merapi (e.g., Wassermann and Ohrnberger, 2001; Ratdomopurbo and Poupinet, 2000).

4 Data

For our study we use data from the amphibious local seismic network which was temporarily deployed on the Indonesian island of Java in 2004 for a period of 150 days from May to October 2004 (Merapi Amphibious Experiment, MERAMEX project, Koulakov et al., 2007; Wagner et al., 2007). The network consisted of 112 continuously running land stations which were equipped with 99 short-period sensors and 13 broadband sensors. These stations were deployed on the whole width of the island at the transition between Central Java and East Java. Sampling frequency of these land stations was 100 sps. The onshore network was complemented offshore by 5 ocean bottom seismometers and 9 ocean bottom hydrophones (OBS/OBH) covering the whole marine forearc down to the deep sea trench (see Figure 3). These marine stations were running at 50 sps for a time period of 18 weeks.

The network observed a large number of local, regional and teleseismic earthquakes. Most of the local earthquakes occur offshore and in the south-coastal region. Manual arrival time picking yielded a dataset of 244 local earthquakes which occurred within the network (5,773 P-phases and 2,120 S-phases). This dataset formed the base for the attenuation study.

5 Method

Attenuation influences the seismic waves traveling from source i to receiver j in the following way (e.g., Sanders, 1993):

$$A_{i,j}(f) = S_j(f)O_j(f)G_{i,j}exp[-\pi f t^*_{i,j}] \quad (1)$$

with S_j: site effect; O_j: source spectrum; G: geometrical spreading; f: frequency. Travel time t and the so-called t^*-operator (path-averaged attenuation) are estimated from the material properties (seismic velocity $v(x, y, z)$ and quality factor $Q(x, y, z)$, respectively) along the ray path between source i and receiver j in a cumulative way:

$$t_{i,j} = \int \frac{dr}{v(x, y, z)} + t_{station} \tag{2}$$

$$t^*_{i,j} = \int \frac{dr}{Q(x, y, z)v(x, y, z)} + t^*_{station} \tag{3}$$

$t_{station}$ and $t^*_{station}$, respectively, are constant station terms.

5.1 t^*-estimation

The path-averaged attenuation $t^*_{i,j}$ can be deduced from the spectra of the seismic observations (equation 1) or more precisely from the spectral fall-off. In our analysis we follow the method outlined in Rietbrock (2001) and Haberland and Rietbrock (2001): Assuming an ω^2 source model (Brune, 1970, 1971; Hanks and Wyss, 1972) we can rewrite equation 1:

$$A_{i,j}(f) = \frac{\Omega_{i,j} exp[-\pi f t^*_{i,j}]}{1 + \frac{f^2}{f^2_{c_i}}} \tag{4}$$

with $\Omega_{i,j}$ being the spectral level (including the source moment, the geometrical spreading and other frequency-independent factors) and f_{c_i} the source corner frequency. In a non-linear spectral inversion technique (spectral fitting) we invert all spectra for the following three free parameters: individual values of $\Omega_{i,j}$ and $t^*_{i,j}$ for each observation, and a (single) value of f_{c_i} common for all observations of an earthquake.

Spectra were automatically calculated for 256 samples (== 2.56 s @ 100 sps) comprising the first part of the direct P-phase arrival using the multitaper approach (Park et al., 1987). For comparison, noise (again 256 samples) directly before the P-arrival was also analyzed. Spectral parameters were determined from continuous portions of the spectra with a signal-to-noise ratio larger than 2. These continuous portions range from 1 Hz to any value between 10 and 30 Hz, depending on signal and noise. Spectra not satisfying these criteria were discarded. We assigned weights between 0 (full weight) and 4 (zero weight) to be used in the tomographic inversion based on the fit of the spectral inversion.

In this study, Q is assumed to be frequency-independent within the small frequency band available. In order to check this assumption we inverted the spectral data also with frequency-dependent $Q(f) = Q_0 f^{\alpha}$, with $0 < \alpha < 1.0$. The data fit is best for $\alpha = 0.0$, although data fit is similarly well for $\alpha < 0.3$. Accordingly, for our data set we assume that Q is frequency-independent. Similar results were also obtained by Rietbrock (2001) for a data set from Japan. However, frequency-dependent Q would be smaller than frequency-independent Q (see also Eberhart-Phillips and Chadwick, 2002).

Figure 4 shows examples of time series and spectra of an arbitrary event. Indications for station specific spectral effects (amplifications of certain frequancies or spectral "holes") can be noticed at some stations, however, most of the spectra follow closely the Brune-type characteristic (see above). Our spectral inversion resulted in 1,929 t^* values of 84 local events which range up to 0.3 s. Analysis of neighboring ray paths (i.e. observations of closely located events with potentially different source corner frequency) yield an average variation of the t^* values of ± 0.01 s. We assume that this value is representative of the average error of the t^* estimates. The S-waves are also affected by

attenuation. Due to the predominant poor signal to noise ratio and generally a smaller number of S-observations, it was not possible to retrieve a sufficient number of t_s^* values for a tomographic inversion. OBH data was not included in the spectral inversion due to the different sensor type.

It is well known that the inversion of single spectra suffers from trade-offs between the corner frequency and the influence of attenuation (e.g., Scherbaum, 1994). The use of a common source corner frequency for all observations of an earthquake introduces an important constraint to the inversion thus allowing for stable and reliable estimates particularly of the t^* values. However, the joint inversion of all observations of an earthquake (as outlined above) works best if a large number of observations of an earthquake is available. As a compromise between data quantity and quality we used a minimum number of observations per event of 6. Nevertheless, tomographic inversions of t^* datasets with a higher minimum number of observations per event (more restrictive) yielded very similar images.

In order to further investigate a possible dependence of the derived t^* values on the estimated source corner frequency (see above), we (artificially) disturbed the derived fc values within the spectral inversion and re-inverted for the plateau value and the individual t^* value. Even if the f_c values are disturbed by random values with a standard deviation of 50% of the original fc values, the influence on the derived t^* values is very minor, i.e. yields average deviations of the t^* values of only 0.01s. The tomographic inversion of the perturbed dataset yields almost identical images as the inversion of the unperturbed dataset thus further corroborating the robustness of the method applied. The source corner frequency seems to be less well resolved which might be due to the expected high values for the small magnitude earthquakes.

The spectral inversion procedure presented above was successfully applied in a series of previous studies (e.g., Rietbrock, 2001; Haberland and Rietbrock, 2001; Eberhart-Phillips and Chadwick, 2002; Schurr et al., 2003) and proved to be very robust.

5.2 Tomographic inversion

For the tomographic inversion (equation 3) we used the computer code SIMUL2000 (Thurber, 1993; Eberhart-Phillips, 1993; Thurber, 1983; Rietbrock, 1996; Evans et al., 1994). The solution is obtained by iterative, damped least squares. The Q_p-model is defined at the intersections of a rectangular grid. Linear B spline interpolation between these grid nodes allow for the continuous spatial variation of the parameter. Intense tests with different grid geometries (i.e. grid spacings) resulted in a final grid spacing of 30 km horizontally and 15 km vertically above 60 km depth (vertical grid spacing of 30 km below 60 km depth; see Figure 4). However, inversions with slightly larger or smaller grid spacing yield basically the same images. Ray-tracing is performed with efficient approximate ray-tracing (ray-bending, Thurber, 1983). The velocity field $v(x, y, z)$ is needed both for accurate ray-tracing and for solving the inversion problem ($Q_p(x, y, z)$ x $v(x, y, z)$; see formulation 3). Based on the travel time picks (see section 3) we calculated the velocity model for the same grid geometry. The resulting velocity model is in good agreement with the models calculated by Koulakov et al. (2007) and Wagner et al. (2007); the main features of the velocity structure in Central Java, particularly the prominent low-velocity anomaly beneath and north of the volcanic arc, are summarized in section 3.

The damping factor (of the damped least squares inversion) was selected according to the analysis of the so-called trade-off curve based on one step inversions with different damping values (following the procedure outlined in Eberhart-Phillips (1986)). This selected damping value of 300 greatly reduces the data variance with only a moderate increase of the model variance. Inversions with different damping values yield similar models with slightly broader or more focused anomalies, and with different absolute amplitudes of the anomalies. However, we found that the overall pattern of anomalies is largely preserved when damping is varied within reasonable limits.

The program code also allows for the inversion of individual station corrections ($t^*_{station}$; see equation 3) which account for small-scale horizontal variations of the very shallow structure beneath the seismic stations (e.g., site effects), particularly for those smaller than the grid node spacing. Damping for the station corrections was set to a relatively high value such that the resulting corrections do not show trends extending over several neighboring stations (i.e. over the horizontal grid node spacing of 30 km), which are better accounted for by regular shallow grid nodes. Most of the positive station corrections are found at stations in the Kendeng Basin and at volcanoes. However, they do not exceed 0.01 s.

In the damped least squares inversion the residuals are minimized in an iterative procedure. Analogous to the velocity tomography case the successive t^* residuals (t^*_{obs} - t^*_{cal}) are calculated using t^*_{cal} values derived from the initial model or the model from the previous iteration, respectively. During the inversion for the Q structure the velocity model is not modified; accordingly, hypocenters are not re-located which stabilizes the whole inversion significantly (t^* data can be treated as shots with known hypocenter coordinates

and origin times). As the initial model we used a homogeneous model; the value of $Q_{p_{hom}} = 600$ is the average of all observed t/t^* values.

6 Resolution of the attenuation model

Due to the irregular and often unfavorable spatial distribution of sources and receivers the study volume is imaged with varying accuracy. Moreover, estimates of path-averaged attenuation (t^*) have larger uncertainties than travel time readings since they are already the product of an inversion process (see above). In recent years different methods have been established to assess the fidelity of the derived models (see references below). We investigate the confidence of our models with analysis of the model resolution matrix and synthetic recovery tests.

6.1 Estimates from resolution matrix

The inversion code provides the model resolution matrix (MRM) describing how well the information is focused in a particular node or smeared into adjacent nodes. The so-called spread function proved to be a useful and compact measure to explore and image the rather bulky MRM (e.g., Toomey and Foulger, 1989; Michelini and McEvilly, 1991). Well resolved model regions should be characterized by small spread values, while unresolved regions have higher spread values. Additionally, contour lines of the elements of each row of the MRM, normalized to the value of the diagonal elements and plotted at their correct spatial position, illustrate possible smearing effects (for details see Eberhart-Phillips and Michael, 1998).

Spread values and 70%-contour lines of the normalized MRM elements for each grid node for 6 north-south depth sections are shown in Figure 6. These sections show spread values up to 2.7 in the center region of the model, that is for most of central and southern part of the island and the marine forearc close to the coast. Here, compact contour lines (smaller or at least not much larger than the grid node spacing) indicate excellent resolution and no smearing down to almost 100 km. Elongated contours are found toward the edges of the model. In the marine forearc these contour lines indicate horizontal smearing (due to predominant horizontal ray paths), in the deeper and northern parts of the model (north of the modern magmatic arc) we notice significant vertical smearing as indicated by vertically elongated contours.

6.2 Synthetic tests

In the recovery tests we set up 3D-synthetic models, calculate the corresponding t^* dataset for the same source and receiver geometry, add random noise and invert this dataset in the same way as the real data. Visual comparison of input model and inverted (output) model allows us to assess the resolution capabilities of the model volume and how well certain (expected) features are imaged in the tomographic inversion.

The synthetic models (Figure 7) consist of a homogeneous background model of Q_p=1,200 and low-Q_p anomalies (Q_p=100) (a) in the upper crust of the island, (b) in the deeper part of the frontal forearc and (c) in the deeper mantle level (see Figure 5). All anomalies stretch over some neighboring grid-nodes. The random noise added to this synthetic t^* dataset has a standard deviation of 0.01 s corresponding to the estimated average uncertainty of the

real t^* values.

The comparison of input and output models (Figure 7) shows the following: Anomalies within the central region (characterized by spread-values < 2.5; see above) are well reproduced in shape; this is particularly true for the upper-crustal anomaly in the center of the island. Here, the amplitude of the anomaly is also well reproduced as is the marine forearc anomaly where it is sampled by crossing rays. We notice some - predominant sub-horizontal - smearing effects for the upper mantle anomalies. The western sub-anomaly is not imaged due to the very limited number of crossing rays.

In a second test (no figure) we introduced a larger anomaly in the mantle beneath the magmatic arc. The reconstructed images clearly show that in this case the resulting anomalies would be much larger. Another test shows that a larger thickness of the crustal anomaly north of the modern magmatic arc could be resolved.

In conclusion, anomalies of comparable size and amplitude as in the synthetic test can be well imaged in the center part of the study region, which is characterized by spread values up to 2.5. Here, the spatial resolution of the model is given by the grid-node spacing. For anomalies in regions with spread values between 2.5 and 3 we have to expect smearing over neighboring grid-nodes

7 Results and Discussion

The results of the tomographic inversions are shown in Figures 8 and 9. Figure 10 provides a summarizing cartoon.

Wide regions of the crust and mantle beneath Java, particularly in the forearc, are characterized by Q_p values higher than 600. Also in the subducting slab - as far as resolved - high to very high Q_p values are found (larger than 600). This is in very good agreement with studies in other subduction zones where similar high Q_p values were observed in the subducting lithosphere (e.g., Stachnik et al., 2004; Tsumura et al., 2000; Haberland and Rietbrock, 2001; Schurr et al., 2003; Eberhart-Phillips and Chadwick, 2002; Eberhart-Phillips et al., 2008; Roth et al., 1999). In addition, a series of anomalies can be noted: Regions of high attenuation are found beneath the central part of Java, beneath and north of the modern magmatic arc, in the deeper mantle beneath Java, and in some patches in the marine forearc.

7.1 Crustal anomalies - sedimentary basin & volcanoes

The strongest Q_p anomalies ($Q_p < 100$) are found in a trench-parallel, though somehow discontinuous, band in the upper crust beneath the center of the island (see Figure 8 and 9). The anomalies are mainly found in upper crustal levels down to 15 km depth. This zone of high attenuation is best developed north of the modern magmatic arc in the eastern part of the study area. The anomaly is not directly located beneath the volcanoes; in fact, most of the volcanoes line up at the edge of the anomaly or anomalies, respectively. This anomaly correlates spatially very well with the negative Bouguer anomaly, and here also the low velocity anomaly is found in this depth range (Koulakov et al., 2007; Wagner et al., 2007, see above). Moreover, at around 110.75°E (i.e. north of Mt. Merapi) this zone exhibits high electrical conductivity (revealed by a magnetotelluric study; Hoffmann-Rothe et al., 2001).

It appears that this upper crustal anomaly has two major contributions, a sedimentary and a magmatic one. We suggest that the eastern part of the low-Q_p anomaly mainly reflects the thick sedimentary deposits of the Kendeng Basin (labelled "A" in Figures 8, 9, and 10). Sedimentary basins are well known for increased attenuation. Hauksson and Shearer (2006) for example found Q_p values of < 200 down to a depth of 10 km in the Ventura basin in California. Li et al. (2006) found high attenuation in the Seattle Basin, Pujades et al. (1997) in the Almeria Basin (Spain). The Kendeng Basin is formed by Eocene to Miocene volcaniclastic turbidites and pelagic mudstones (Smyth et al., 2007; Hall et al., 2007). Clements et al. (2009) point out that - in contrast to basins in Western and Central Java - in Eastern Java "most of the basin fill came from the volcanic arc to the South, which for much of the Oligocene and Early Miocene was emergent and explosive, providing immense amounts of volcanic debris and abundant volcanic quartz". The large basin thickness might in part be due to arc loading as proposed by Waltham et al. (2008). Evidence for fluid saturation of the Kendeng Basin sediments and for overpressure come from mud volcanoes which are found in East Java (e.g., Clements et al., 2009). These mud volcanoes are located in the Western part of the Kendeng Basin (e.g., Sangiran Dome; Lunt et al., 1998) and also in the East at the western margin of the Strait of Madura, where the Lusi mud volcano formed in 2006 and erupted up to 180,000m^3 of mud each day (e.g., Mazzini et al., 2007). Clements et al. (2009) point out that mud volcanoes are "(...) the surface expressions of overpressure which commonly reflects rapid sedimentation or thrusting". Currently, the Kendeng Basin is under compression and is today a fold- and thrust belt (e.g., de Genevraye and Samuel, 1972). It is likely that the high content of overpressured fluids in the thick sediment fill of the Kendeng Basin is mainly responsible for the strong shallow Q_p anomaly in the

north-eastern part of the study area.

However, we notice reduced Q_p values also in the upper crust outside of the Kendeng Basin ("B" in Figures 8). Here, the reduced Q_p values are in the direct vicinity of Mt. Sumbing, Mt. Sundoro, and the Dieng volcanic complex. Furthermore, beneath Mt. Merapi the low-Q_p anomaly extends down to 35 km depth which is clearly below the expected depth of the Kendeng Basin, and we notice a southward dip of the anomaly in some cross sections (see Figure 8).

Hence, we interpret the lower part of these upper- to mid-crustal anomalies to reflect elevated temperatures and possibly partial melts and magma chambers directly beneath the volcanic centers ($<$ 15 km to 35 km depth; "B" in Figures 8, 9, and 10). Also Koulakov et al. (2007) and Wagner et al. (2007) interpreted the coinciding low v_p anomaly as due to magmatic processes. Recent studies suggest that at Mt. Merapi significant quantities of CO_2 were added from shallow crustal sources (Troll et al., 2012). Reduced Q_p is often found in volcanic areas in the crust (e.g., Haberland and Rietbrock, 2001; Young and Ward, 1980; Evans and Zucca, 1988; Ho-Liu et al., 1988; Clawson et al., 1989; Ponko and Sanders, 1994; Romero et al., 1997). However, based on the tomographic images it is difficult to exactly differentiate between the two contributions.

In the mid crust to lower crust no enhanced attenuation is found throughout the modern arc. This indicates that these levels are not associated with strong heating of the (lower) crust and the generation of voluminous partial melts beneath the volcanic arc. In this context it is interesting to note that geochemical observations suggest, that most of the Sunda Arc stratovolcanoes "... are the products of relatively primitive subduction melts having no significant interaction with the underlying crust" (Smyth et al., 2007; Nicholls and

Whitford, 1983; Wheller et al., 1987).

These conditions are remarkably different to the images from the central Andes, where in regions of late Neogene silicic magmatism the whole thickened crust (from the surface to the crustal base) is characterized by extremely high attenuation (with $Q_p < 100$; Haberland and Rietbrock, 2001; Haberland et al., 2003; Schurr et al., 2003). In these regions of the Altiplano-Puna volcanic zone these extreme anomalies of low Q_p values were interpreted to reflect the partially molten crust, elevated temperatures and fluid pathways from the deeper levels of the subduction zone. In parts of the Central Andean arc without young silicic magmatism only moderate Q_p values in the crust were found. The Q_p distribution found in Central/East Java (this study) resembles much better the Q_p distribution in these segments of the central Andes.

It is interesting to note that enhanced attenuation is also found in the crust at around 15 km in an elongated anomaly toward Mt. Lasem, a Quaternary potassic calc-alcaline volcano (Leterrier et al., 1990). However, this anomaly is already at the edge of the network and the model here is less well resolved.

7.2 Forearc and plate interface

Most of the forearc is characterized by moderate to high Q_p values (low attenuation). However, in two patches in the outer forearc directly above (or within) the oceanic crust increased attenuation is found in a depth range of 30 to 50 km ("C" in Figures 8, 9, and 10). The trench-ward limit seems not to be resolved. In these patches we also notice increased seismic activity which most likely takes place at the plate interface and within the forearc crust.

We suggest that the high attenuation observed in our study is an indication for fluids circulating in the subducted sediments and in the overlying forearc. Here, we expect a fluid expulsion from the subducting plate (e.g., Hyndman et al., 1997), both from dehydration reactions within the oceanic crust (which was hydrated on its way from the spreading ridge into the trench; e.g. Ranero et al., 2008) and from the sediments on top of the oceanic crust which are down-dragged in the subduction process (subduction channel, e.g., Cloos and Shreve, 1988) and become compacted with increasing depth. The liberated fluids can then drain through the fractured upper plate or migrate along the decollement toward the deformation front (e.g., Ranero et al., 2008). Also in parts of the Raukumura Peninsula (Hikurangi subduction zone, New Zealand) a zone of low Q_p had been observed above the subduction plate at a depth of 20 to 40 km which had been interpreted as sediments subducted and ponded at the base of the forearc (Eberhart-Phillips and Chadwick, 2002).

The v_p/v_s ratios are also often indicative of high fluid saturation. In South-Central Chile Haberland et al. (2007) found strongly increased v_p/v_s ratios in the forearc reflecting young, fluid-saturated sediments of forearc basins and of the accretionary prism. Evidence for fluids released into the forearc after a strong interplate earthquake in northern Chile (in other subduction zones) was provided by v_p/v_s models (Husen and Kissling, 2001) and high-precision relocation of aftershocks (Nippress and Rietbrock, 2007).

Off Central Java increased v_p/v_s ratios are found at a depth between 5 and 25 km (Koulakov et al., 2007) further corroborating a high fluid saturation at least of parts of the forearc. However, both v_p/v_s and Q_p anomalies are at the edge of the model and thus not well resolved.

7.3 Mantle wedge

Elevated attenuation values are observed in the mantle, directly beneath the magmatic arc, at around 100 km depth and directly above the subducting plate. Here we reach Q_p values down to 100 ("D" in Figures 8, 9, and 10).

These anomalies are interpreted to reflect the location of melt generation in the mantle wedge beneath the magmatic arc. According to petrophysical models, the addition of volatiles in the asthenosphere above the slab (at around 100 km depth) is considered to be responsible for the generation of basaltic melts in the mantle wedge (e.g., Tatsumi, 1986, 1989; Tatsumi and Eggins, 1995; Davies and Stevenson, 1992; Peacock, 1996). However, the exact mechanism of fluid release and how they are transported to this location are still disputed (for discussion see e.g. Stern, 2002).

Nevertheless, we note that the regions of elevated attenuation in the mantle beneath Java are relatively small and patchy, and that elevated attenuation is not found in a larger region beneath the arc (or backarc) as it is found in many subduction zones (see Table 1). Tsumura et al. (2000) found varying Q in the mantle wedge in the north-eastern Japan arc and related it to different volcanic activity (low Q corresponding to high volcanic activity and vice versa). Our synthetic tests confirm that we could have resolved a larger attenuating mantle region (see above).

It is conceivable that this characteristic of Java is related to the low intermediate seismicity which can be observed in this subduction zone segment (see also Figure 1). According to the conceptual model by Kirby et al. (1996) increased intermediate depth seismicity indicates locations of increased fluid

Table 1: Subduction zone with large low-Q region beneath arc or backarc (selection)	Reference
Alaska	Stachnik et al. (2004)
Central Chile	Haberland and Rietbrock (2001); Schurr et al. (2003)
Central Mexico	Chen and Clayton (2009)
Marianas	Pozgay et al. (2009)
Northern Apennines	Piccinini et al. (2010)
Southern Apennines-Calabrian Arc	Monna and Dahm (2009)
Central North Island, New Zealand	Eberhart-Phillips et al. (2008)

release which in turn could yield in an increased melt generation. To further check this hypothesis it would be favourable to make additional seismic investigations covering those segments of the Sunda subduction zone showing increased intermediate depth seismicity.

8 Conclusions

We successfully applied a spectral inversion technique to derive path-average attenuation estimates (t^*) for a large number of P-wave recordings of the MERAMEX data set which were then used to calculate tomographic images of attenuation (Q_p) in the crust and upper mantle. The tomographic images provide a detailed insight into the tectonic and magmatic processes in the

Java subduction zone. Similar to investigations in other subduction zones, our findings seem to confirm that the distribution of seismic attenuation images fluid related processes. The main findings can be summarized as follows:

- The strongest Q_p anomaly (< 100) is found in upper- to mid-crustal levels in a trench-parallel band in the center of East and Central Java. The eastern part of this low Q_p anomaly correlates spatially very well with the Kendeng Basin (known from surface geological mapping), also indicated by a low v_p and v_s anomaly, and a strong negative Bouguer anomaly. We suggest that the anomalous Q_p values in the eastern part of the study area (down to a depth of 15 km) are mainly caused by the thick and fluid-saturated sediments of the Kendeng Basin .
- Most of the active volcanoes are located at the edges of the low Q_p anomaly in the upper crust, and often there is low Q_p found in direct vicinity of the volcanic centres. The anomalies suggest that partial melts, elevated temperatures and fluids are found in upper-crustal levels (particluarly beneath Mt. Merapi down to 30 km depth).
- High attenuation is not found throughout the crust beneath the active magmatic arc. This suggests that the deeper levels are not associated with strong heating of the (lower) crust and the generation of voluminous partial melts beneath the volcanic arc. This observation is similar to observations along segments of the central Andean arc without young silicic volcanism.
- Generally moderate attenuation in the mantle wedge beneath the volcanic arc might be due to a low rate of intermediate depth seismicity in this subduction zone segment.
- The low Q_p anomalies above the subducting slab in the marine forearc possibly reflect zones of increased fluid content from the subduction channel.

Acknowledgements

MERAMEX data were kindly provided by the Seismological Data Archive/ GEOFON of the GFZ Potsdam. The instruments were supplieded by the Geophysical Instrument Pool Potsdam (GIPP) of the GFZ, the Christian Albrecht University, Kiel and the IFM-GEOMAR, Kiel. The project was financed by the German BMBF and DFG within the R&D programme GEOTECHNOLOGIEN. Essential logistical support of the project was provided by the Volcanological Survey of Indonesia (VSI) Bandung, the Volcanological Technologicy Research Center (BPPTK) Yogyakarta, the Gadjah Mada University (UGM) Yogyakarta and the Meteorological and Geophysical Agency (BMG) Jakarta. We thank all field crews for their great work related with station installation, and many landowners for allowing us to deploy the equipment on their property; the master and crew of RV Sonne (SO 176 and SO 179) for the offshore deployment. Philippe Jousset provided helpful comments on the manuscript. We thank reviewers Helen Smyth and Nick Rawlinson for their valuable suggestions which significantly improved the paper. All figures were made using the GMT software code (Wessel and Smith, 1998). The Bureau Gravimetrique International (BGI) / International Association of Geodesy kindly provided the Bouguer gravity data.

References

Aki, K., Richards, P. G., 1980. Quantitative Seismology. W.H. Freeman and Co., USA.

Ammon, C. J., Kanamori, H., Lay, T., Velasco, A. A., 2006. The

17 July 2006 Java tsunami earthquake. Geophys. Res. Lett. 33, doi: 10.1029/2006GL028005.

Barazangi, M., Isacks, B., 1971. Lateral variations of seismic-wave attenuation in the upper mantle above the inclined earthquake zone of the Tonga island arc: Deep anomaly in the upper mantle. J. Geophys. Res. 76, 8.493–8.516.

Barazangi, M., Pennington, W., Isacks, B., 1975. Global study of seismic wave attenuation in the upper mantle behind island arcs using pP waves. J. Geophys. Res. 80, 1079–1092.

Brune, J. N., 1970. Tectonic stress and the spectra of seismic shear waves from earthquakes. J. Geophys. Res. 75 (26), 4997–5009.

Brune, J. N., 1971. Correction. J. Geophys. Res. 76 (20), 5002.

Chen, T., Clayton, R. W., 2009. Seismic attenuation structure in central Mexico: Image of a focused high-attenuation zone in the mantle wedge. J. Geophys. Res. 114, B07304, doi:10.1029/2008JB005964.

Chinn, D. S., Isacks, B. L., Barazangi, M., 1980. High-frequency seismic wave propagation in western South America along the continental margin, in the Nazca plate and across the Altiplano. Geophys. J. R. Astr. Soc. 60, 209–244.

Clawson, S. R., Smith, R. B., Benz, H. M., 1989. P wave attenuation of the Yellowstone Caldera from three-dimensional inversion of spectral decay using explosion source seismic data. J. Geophys. Res. 94, 7.205–7.222.

Clements, B., Hall, R., Cottam, M. Q., 2009. Thrusting a volcanic arc: a new structural model for Java. Petroleum Geoscience 15, 159–174.

Cloos, M., Shreve, R. L., 1988. Subduction-channel model of prism accretion, melange formation, sediment subduction, and subduction erosion at convergent plate margins: 1. background and description. Pure and Applied Geophysics 128, 455–500, 10.1007/BF00874548.

Davies, J. H., Stevenson, D., 1992. Physical model of source region of subduc-

tion zone volcanics. J. Geophys. Res. 97 (B2), 2037–2070.

de Genevraye, P., Samuel, L., 1972. The geology of the Kendeng Zone (East Java). Indonesian Petroleum Association, Proceedings 1st Annual Convention, 17–30.

Eberhart-Phillips, D., 1986. Three-dimensional structure in northern California coast ranges from inversion of local earthquake arrival times. Bull. Seismol. Soc. Am. 76 (4), 1025–1052.

Eberhart-Phillips, D., 1993. Local earthquake tomography: Earthquake source regions. In: Iyer, H., Hirahara, K. (Eds.), Seismic Tomography: Theory and Practice. Chapman and Hall, New York, pp. 613–643.

Eberhart-Phillips, D., Chadwick, M., 2002. Three-dimensional attenuation model of the shallow Hikurangi subduction zone in the Raukumara Peninsula, New Zealand. J. Geophys. Res. 107 (B2), 2033.

Eberhart-Phillips, D., Chadwick, M., Bannister, S., 2008. Three-dimensional attenuation structure of central and southern south island, new zealand, from local earthquakes. J. Geophys. Res. 113, B05308.

Eberhart-Phillips, D., Michael, A. J., 1998. Seismotectonics of the Loma Prieta, California, region determined from three-dimensional v_p, v_p/v_s, and seismicity. J. Geophys. Res. 103 (B9), 21,099–21,120.

Edwards, C., Menzies, M., Thirlwall, M., 1991. Evidence from Muriah, Indonesia, for the Interplay of supra-subduction zone and intraplate processes in the genesis of potassic alcaline magmas. J. Petrol. 32 (3), 555–592.

Evans, J., Eberhart-Phillips, D., Thurber, C. H., 1994. User's manual for simulps12 for imaging $\underline{\mathrm{v}_p}$ and $\underline{\mathrm{v}_p/\mathrm{v}_s}$: A derivative of the "Thurber" tomographic inversion simul3 for local earthquakes and explosions. Open File Rep. 94-431, U.S. Geol. Surv.

Evans, J. R., Zucca, J. J., 1988. Active high-resolution seismic tomography

of compressional wave velocity and attenuation structure at Medicine Lake Volcano, Northern California Cascade Range. J. Geophys. Res. 93, 15.016–15.036.

Gill, J. B., 1981. Orogenic Andesites and Plate Tectonics. Springer-Verlag, Berlin.

Haberland, C., Rietbrock, A., 2001. Attenuation tomography in the western central Andes: a detailed insight into the structure of a magmatic arc. J. Geophys. Res. 106, 11.151–11.167.

Haberland, C., Rietbrock, A., Lange, D., Bataille, K., Dahm, T., 2007. Structure of the seismogenic zone of the southcentral Chilean margin revealed by local earthquake traveltime tomography. J. Geophys. Res. 114, B01317.

Haberland, C., Rietbrock, A., Schurr, B., Brasse, H., 2003. Coincident anomalies of seismic attenuation and electrical resistivity beneath the southern bolivian altiplano plateau. Geophys. Res. Lett. 30 (18), 1923.

Hall, R., Clements, B., Smyth, H. R., Cottam, M. A., 2007. A New interpretation of Java's structure. In: Proceedings Indonesian Petroleum Association, 31st Annual Convention and Exhibition. pp. 63–86.

Hanks, T. C., Wyss, M., 1972. The use of body-wave spectra in the determination of seismic-source parameters. Bull. Seismol. Soc. Am. 62 (2), 561–589.

Hashida, T., 1989. Three-dimensional seismic attenuation structure beneath the Japanese Islands and its tectonic and thermal implications. Tectonophysics 159, 163–180.

Hauksson, E., Shearer, P. M., 2006. Attenuation models (Q_p and Q_s) in three dimensions of the southern California crust: Inferred fluid saturation at seismogenic depths. J. Geophys. Res. 111, B05302, doi:10.1029/2005JB003947.

Ho-Liu, P., Kanamori, H., Clayton, R. W., 1988. Applications of attenuation tomography to Imperial Valley and Coso-Indian Wells region, southern Cal-

ifornia. J. Geophys. Res. 93 (B9), 10,501–10,520.

Hoffmann-Rothe, A., Ritter, O., Haak, V., 2001. Magnetotelluric and geomagnetic modelling reveals zones of very high electrical conductivity in the upper crust of Central Java. Phys. Earth Planet. Inter. 124, 131–151.

Hoshiba, M., Rietbrock, A., Scherbaum, F., Nakahava, H., Haberland, C., 2001. Scattering attenuation and intrinsic absorption in northern Chile using full seismogram envelope. Seismology 5(2), 157–179.

Husen, S., Kissling, E., 2001. Postseismic fluid flow after the large subduction earthquake of Antofagasta, Chile. Geology 29 (9), 847–850.

Hyndman, R., Yamano, M., Oleskevich, D., 1997. The seismogenic zone of subduction thrust faults. The Island Arc 6, 244–260.

Hyndman, R. D., Peacock, S. M., 2003. Serpentinization of the forearc mantle. Earth Plan. Sci. Lett. 212 (3-4), 417–432.

Jackson, I., Fitz Gerald, J. D., Faul, U. H., Tan, B. H., 2002. Grain-size-sensitive seismic wave attenuation in polycrystalline olivine. J. Geophys. Res. 107, No. B12, 2360, doi:10.1029/2001JB001225.

Johnston, D., Toksös, M., Timor, A., 1979. Attenuation of seismic waves in dry and saturated rocks, II, Mechanisms. Geophysics 44 (4), 691–711.

Karato, S., Spetzler, H. A., 1990. Defect microdynamics in minerals and solid-state mechanisms of seismic wave attenuation and velocity dispersion in the mantle. Rev. of Geophys. 28, 399–421.

Kirby, S., Engdahl, E. R., Denlinger, R., 1996. Intermediate-depth intraslab earthquakes and arc volcanism as physical expressions of crustal and uppermost mantle metamorphism in subducting slabs (overview). In: Bebout, G. E., Scholl, D. W., Kirby, S. H., Platt, J. P. (Eds.), Subduction: Top to Bottom, Geophys. Monogr. Ser., vol. 96. AGU, Washington, D.C., pp. 195–214.

Kopp, H., 2011. The Java convergent margin: structure, seismogenesis and subduction processes. In: Hall, R., Cottam, M. A., Wilson, M. E. J. (Eds.), The SE Asian gateway: History and Tectonics of the Australia-Asia Collision. Geological Society of London, Special Publications 355, pp. 111–137, doi:10.1144/SP355.6.

Koulakov, I., Bohm, M., Asch, G., Lhr, B., Manzanares, A., Brotopuspito, K., Fauzi, P., Purbawinata, M., Puspito, N., Ratdomopurbo, A., Kopp, H., und E. Shevkunova, W. R., 2007. P and s velocity sturcture of the crust and the upper mantle beneath Central Java from local tomography inversion. J. Geophys. Res. 112 (B8), B08310.

Koulakov, I., Jakovlev, A., Luehr, B. G., 2009. Anisotropic structure beneath central Java from local earthquake tomography. Geochem. Geophys. Geosyst. 10 (2).

Leterrier, J., Yuwono, Y. S., Soeria-Atmadja, R., Maury, R. C., 1990. Potassic volcanism in Central Java and South Sulawesi, Indonesia. Journal of Southeast Asian Earth Sciences 4 (3), 171–187.

Li, Q., Wilcock, W. S. D., Pratt, T. L., Snelson, C. M., Brocher, T. M., 2006. Seismic Attenuation Structure of the Seattle Basin, Washington State, from Explosive-Source Refraction Data. Bull. Seismol. Soc. Am. 96 (2), 553–571, doi: 10.1785/0120040164.

Lunt, P., Netherwood, R., Huffman, O. F., 1998. IPA Field Trip to Central Java. Fieldtrip Guidebook. Indonesian Petroleum Association, Jakarta, Indonesia.

Mavko, G. M., 1980. Velocity and attenuation in partially molten rocks. J. Geophys. Res. 85 (B10), 5173–5189.

Mavko, G. M., Nur, A., 1975. Melt squirt in the asthenosphere. J. Geophys. Res. 80 (11), 1.444–1.448.

Mazzini, A., Svensen, H., Akhmanov, G. G., Aloisi, G., Planke, S., A. Malthe-Sørenssen, Istadi, B., 2007. Triggering and dynamic evolution of LUSI mud volcano, Indonesia. Earth Plan. Sci. Lett. 261, 375–388, doi: 10.1016/j.epsl.2007.07.001.

Michelini, A., McEvilly, T., 1991. Seismological studies at Parkfield. I. Simultaneous inversion for velocity structure and hypocenters using cubic B-splines parameterization. Bull. Seismol. Soc. Am. 81 (2), 524–552.

Monna, S., Dahm, T., 2009. Three-dimensional P wave attenuation and velocity upper mantle tomography of the southern Apennines - Calabrian Arc subduction zone. J. Geophys. Res. 114,B06304, doi:10.1029/2008JB005677.

Newcomb, K., McCann, W. R., 1987. Seismic history and seismotectonics of the Sunda Arc. J. Geophys. Res. 92 (B1), 421–439.

Nicholls, I., Whitford, D., 1983. Potassium-rich volcanic rocks of the Muriah complex, Java, Indonesia: Products of multiple magma sources? Journal of Volcanology and Geothermal Research 18 (1ŏ20134), 337 – 359.

Nippress, S., Rietbrock, A., 2007. Seismogenic zone high permeability in the Central Andes inferred from relocations of micro-earthquakes. Earth Plan. Sci. Lett. 263, 235–245.

Park, J., Lindberg, C. R., Vernon, F. L., 1987. Multitaper spectral analysis of high-frequency seismograms. J. Geophys. Res. 92, 12,675–12,684.

Peacock, S. A., 1990. Fluid processes in subduction zones. Science 248 (4953), 329–337.

Peacock, S. M., 1996. Thermal and petrologic structure of subduction zones (overview). In: Bebout, G. E., Scholl, D. W., Kirby, S. H., Platt, J. P. (Eds.), Subduction: Top to Bottom, Geophys. Monogr. Ser., vol. 96. AGU, Washington, D.C., pp. 119–133.

Piccinini, D., Di Bona, M., Lucente, F. P., Levin, V., Park, J., 2010. Seismic

attenuation and mantle wedge temperature in the northern Apennines subduction zone (Italy) from teleseismic body wave spectra. J. Geophys. Res. 115, B09309, doi: 10.1029/2009JB007180.

Ponko, S. C., Sanders, C. O., 1994. Inversion for P and S wave attenuation structure, Long Valley caldera, California. J. Geophys. Res. 99 (B2), 2.619–2.635.

Pozgay, S. H., Wiens, D. A., Conder, J. A., Shiobara, H., Sugioka, H., 2009. Seismic attenuation tomography of the mariana subduction system: Implications for thermal structure, volatile distribution, and slow spreading dynamics. Geochem. Geophys. Geosyst. 10, Q04X05.

Pujades, L. G., Ugalde, A., Canas, J. A., Navarro, M., Badal, F. J., Corchete, V., 1997. Intrinsic and scattering attenuation from observed seismic codas in the Almeria Basin (southeastern Iberian Peninsula). Geophys. J. Int. 129 (2), 281–291, doi: 10.1111/j.1365-246X.1997.tb01581.x.

Ranero, C., Grevemeyer, I., Sahling, H., Barckhausen, U., Hensen, C., Wallmann, K., Weinrebe, W., Vannucchi, P., von Huene, R., McIntosh, K., 2008. Hydrogeological system of erosional convergent margins and its influence on tectonics and interplate seismogenesis. Geochem. Geophys. Geosyst. 9, Q03S04.

Ranero, C., Morgan, J., McIntosh, K., Reichert, C., 2003. Bending-related faulting and mantle serpentinization at the middle americ trench. Nature 425, 367–373.

Ratdomopurbo, A., Poupinet, G., 2000. An overview of the seismicity of Mmerapi volcano (Java, Indonesia), 1983-1994. Journal of Volcanology and Geothermal Research 100 (1-4), 193 – 214.

Rietbrock, A., 1996. Entwicklung eines Programmsystems zur konsistenten Auswertung grosser seismologischer Datensätze mit Anwendung auf die Un-

tersuchung der Absorptionsstruktur der Loma-Prieta-Region, Kalifornien. Ph.D. thesis, Ludwig-Maximilians-Universität, Munich, Germany.

Rietbrock, A., 2001. P wave attenuation structure in the fault area of the 1995 Kobe earthquake. J. Geophys. Res. 106, 4.141–4.154.

Romero, A. E., McEvilly, T. V., Majer, E. L., 1997. 3-D microearthquake attenuation tomography at the Northwest Geysers geothermal region, California. Geophysics 62 (1), 149–167.

Roth, E. G., Wiens, D. A., Dorman, L. M., Hildebrand, J., Webb, S. C., 1999. Seismic attenuation tomography of the Tonga-Fiji region using phase pair method. J. Geophys. Res. 104 (B3), 4.795–4.809.

Sacks, I. S., Okada, H., 1974. A comparison of the anelasticity structure beneath western South America and Japan. Phys. Earth Planet. Inter. 9, 211–219.

Saffer, D. M., Tobin, H. J., 2011. Hydrogeology and mechanics of subduction zone forearcs: Fluid flow and pore pressure. Annual Review of Earth and Planetary Sciences 39 (1), 157–186.

Sanders, C. O., 1993. Local earthquake tomography: attenuation – theory and results. In: Iyer, H., Hirahara, K. (Eds.), Seismic Tomography: Theory and Practice. Chapman and Hall, New York, pp. 676–694.

Satake, K., Hashida, T., 1989. Three-dimensional attenuation structure beneath North Island, New Zealand. Tectonophysics 159, 181–194.

Sato, H., Sacks, I. S., Murase, T., Muncill, G., Fukuyama, H., 1989. Q_p-melting temperature relation in peridotite at high pressure and temperature: Attenuation mechanism and implications for the mechanical properties of the upper mantle. J. Geophys. Res. 94 (B8), 10,647–10,661.

Scherbaum, F., 1994. Modelling the Roermond earthquake of 1992 April 13 by stochastic simulation of its high-frequency strong ground motion. Geophys.

J. Int. 119, 31–43.

Schurr, B., Asch, G., Rietbrock, A., Trumbull, R., Haberland, C., 2003. Complex patterns of fluid and melt transport in the central andean subduction zone revealed by attenuation tomography. Earth and Planetary Science Letters 215 (1ŏ20132), 105 – 119.

Simandjuntak, T. O., Barber, A. J., 1996. Contrasting tectonic styles in the Neogene orogenic belts of Indonesia. In: Hall, R., Blundell, D. J. (Eds.), Tectonic evolution of Southeast Asia. Vol. 106. Geological Society of London, London, pp. 185–201.

Smyth, H., Hall, R., Hamilton, J., Kinny, P., 2005. East java: Cenozoic basins, volcanoes and ancient basement. Indonesian Petroleum Association, Proceedings 30th Annual Convention, 251–266IPA05-G-045.

Smyth, H. R., Hall, R., Nichols, G. J., 2008. Cenozoic volcanic Arc history of east Java, Indonesia: The stratigraphic record of eruptions on an active continental margin. In: Draut, A. E., Clift, P. D., Scholl, D. W. (Eds.), Formation and Applications of the Sedimentary Record in Arc Collision Zones. Vol. 436. Geological Society of America Special Paper, pp. 199–222, doi:10.1130/2008.2436(10).

Smyth, H. R., Hamilton, P. J., Hall, R., Kinny, P. D., 2007. The deep crust beneath island arcs: Inherited zircons reveal a Gondwana continental fragment beneath East Java, Indonesia. Earth Plan. Sci. Lett. 258, 269–282.

Stachnik, J. C., Abers, G. A., Christensen, D. H., 2004. Seismic attenuation and mantle wedge temperatures in the alaska subduction zone. J. Geophys. Res., 109.

Stern, R. J., 2002. Subduction zones. Rev. Geophys. 40 (4), 38.

Tatsumi, Y., 1986. Formation of the volcanic front in subduction zones. Geophys. Res. Lett. 13 (8), 717–720.

Tatsumi, Y., 1989. Migration of fluid phases and genesis of basalt magmas in subduction zones. J. Geophys. Res. 94 (B4), 4697–4707.

Tatsumi, Y., Eggins, S., 1995. Subduction Zone Magmatism. Blackwell Sci., Malden, Mass.

Thurber, C., 1983. Earthquake locations and three-dimensional crustal structure in the Coyote Lake area, central California. J. Geophys. Res. 88, 8226–8236.

Thurber, C., 1993. Local earthquake tomography: Velocities and v_p/v_s-theory. In: Iyer, H., Hirahara, K. (Eds.), Seismic Tomography: Theory and Practice. Chapman and Hall, New York, pp. 563–583.

Toomey, D., Foulger, G., 1989. Tomographic inversion of local earthquake data from the Hengill-Grensdalur central volcano complex, Iceland. J. Geophys. Res. 94, 17,497–17,510.

Troll, V., Hilton, D. R., Jolis, E. M., Chadwick, J. P., Blythe, L. S., Deegan, F. M., Schwarzkopf, L. M., Zimmer, M., 2012. Crustal CO2 liberation during the 2006 eruption and earthquake events at Merapi volcano, indonesia. Geophys. Res. Lett. 39, L11302.

Tsumura, N., Matsumoto, S., Horiuchi, S., Hasegawa, A., 2000. Three-dimensional attenuation structure beneath the northeastern japan arc estimated from spectra of small earthquakes. Tectonophysics 319 (4), 241 – 260.

Untung, M., Sato, Y., 1978. Gravity and geological studies in Java, Indonesia. Geological Survey of Indonesia and Geological Survey of Japan, Special Publication.

Van Bemmelen, R., 1949. The geology of Indonesia. Staatsdrukkerij/Nijhoff, Den Haag.

Wagner, D., Koulakov, I., Rabbel, W., Luehr, B.-G., Wittwer, A., Kopp, H.,

Bohm, M., Asch, G., MERAMEX Scientists, 2007. Joint inversion of active and passive seismic data in central java. Geophys. J. Int. 170, 923ŭ2013932.

Waltham, D., Hall, R., Smyth, H. R., Ebinger, C. J., 2008. Basin formation by volcanic arc loading. In: Draut, A. E., Clift, P. D., Scholl, D. W. (Eds.), Formation and Applications of the Sedimentary Record in Arc Collision Zones. Geological Society of America Special Paper 436, pp. 11–26, doi: 10.1130/2008.2436(02).

Wassermann, J., Ohrnberger, M., 2001. Automatic hypocenter determination of volcano induced seismic transients based on wave field coherence - an application to the 1998 eruption of Mt. Merapi, Indonesia. Journal Volcanol. Geoth. Res. 110, 57–77.

Wessel, P., Smith, W., 1998. New, improved version of the Generic Mapping Tools released. suppl. to EOS, Transactions, AGU 79, 579.

Wheller, G., Varne, R., Foden, J., Abbott, M., 1987. Geochemistry of quaternary volcanism in the sunda-banda arc, indonesia, and three-component genesis of island-arc basaltic magmas. Journal of Volcanology and Geothermal Research 32 (1ŭ20133), 137 – 160.

Whitman, D., Isacks, B., Chatelain, J.-L., Chiu, J.-M., Perez, A., 1992. Attenuation of high-frequency seismic waves beneath the central Andean plateau. J. Geophys. Res. 97, 19,929–19,947.

Winkler, K. W., Murphy, W. F., 1995. Acoustic velocity and attenuation in porous rocks. In: Ahrens, T. J. (Ed.), Rock Physics and Phase Relations: A Handbook of Physical Constants. Vol. 3. AGU Reference Shelf, Washington D.C., pp. 20–34.

Wu, H., Lees, J. M., 1996. Attenuation structure of Coso geothermal area, California, from pulse widths. Bull. Seismol. Soc. Am. 86 (5), 1574–1590.

Young, C.-Y., Ward, R., 1980. Three-dimensional Q^{-1} model of the Coso hot

springs known geothermal resource area. J. Geophys. Res. 85, 2.459–2.470.

Fig. 1. Tectonic setting at the Sundaland continental margin. Earthquakes (global catalog) are shown as black dots, volcanoes by black triangles. The study area is outlined by the red rectangle. See text for details.

Fig. 2. Geological Units in the study area in East/Central Java (after Smyth et al., 2008). Modern magmatic arc (Sunda Arc) is indicated by darkest shading with young volcanoes numbered (1: Dieng volcanic complex; 2: Mt. Sundoro; 3: Mt. Sumbing; 4: Mt. Ungaran; 5: Mt. Telomoyo; 6: Mt. Merbabu; 7: Mt. Merapi; 8: Mt. Muria; 9: Mt. Lawu; 10: Mt. Lasem; 11: Mt. Wilis). Dotted line is Muria-Progo lineament (Smyth et al., 2008); white dashed line indicates the 0mGal contour of the negative Bouguer gravity anomaly (min. -58mGal) indicating the thickest part of the Kendeng Basin.

Fig. 3. Distribution and geometry of seismic events (used in attenuation study), volcanoes, stations, and grid nodes. Rays are indicated by gray solid lines. Numbers give x and y coordinates of the grid nodes used in km. Note that OBH stations were not used for the attenuation analysis.

Fig. 4. Time series (top of each panel) and amplitude spectra (bottom of each panel) of the signal and noise portion of recordings at 6 stations of an arbitrary event (2004.05.31,23:09:37.34 UTC). The time windows (signal and noise) used in the frequency analysis are marked in light gray and dark gray, respectively. Signal spectra are shown by the black line, noise spectra by black dashed line, and best fit model by thick gray line. Station names, travel time t, t^* values, assigned weight w as indicated. See text for more details.

Fig. 5. Spatial distribution of (color-coded) path-averaged attenuation values (t/t^*) for an arbitrary event plotted on the station location (2004.09.27, 23:46:24.38 UTC; epicenter indicated by black star). Note consitently high path-averaged attenuation values in most of the forearc (indicated by purple colors) and low path-averaged attenuation values in the center and toward the north (blue and turquise colors).

Fig. 6. Resolution of the model as indicated by the distribution of spread values and 70% contour lines along north-south cross-sections. X-position of section is indicated in the lower left corner of each plot; for position see inset and Figure 3. Spread function is color coded; darker colors indicate better resolved regions; inverted triangle indicate the position of the coastline, black triangles indicate young volcanoes. White line denotes region with spread= 2.7. See text for details.

Fig. 7. 3D-synthetic recovery test: left panel: synthetic model; right panel: resulting model after inversion of synthetic data. X-position of section is indicated in the lower left corner of each plot; for position see inset and Figure 3. Attenuation (Q_p) is color coded; unresolved regions (right panels) are not shown, regions with spread values above 2.5 are shown faded (inn right panel) or indicated by white line (left panels), respectively. Grid nodes are denoted by crosses. Inverted triangle indicate the position of the coastline, black triangles show young volcanoes. See text for details.

Fig. 8. Results of tomographic inversions. Shown are roughly north-south cross sections at x-positions indicated in the lower left corner of each panel (sorted from West to East). For exact position of sections see inset and Figure 3. Attenuation (Q_p) is color coded; regions with spread values above 2.5 are shown faded, unresolved regions are not shown. The black line indicates the inferred approximate top of the subducting slab (based on hypocenter position). Black triangles indicate modern volcanoes; inverted triangle indicate the position of the coastline. White circles indicate hypocenter.

Fig. 9. Results of tomographic inversions. Shown are map views of the tomographic model at different depth (indicated in lower left corner of each panel). The white dashed line depicts the 0mGal contour of the Bouguer anomaly (minimum in the center -58mGal). Black line indicates coast line. Anything else as in Figure 8.

Fig. 10. Interpretative Sketch. Indicated are all features discussed in the text: "A": Anomaly related to sedimentary basin; "B": Volcano- or magma-related anomalies; "C": Anomaly in the marine forearc; "D": Mantle wedge-anomaly. Dashed line (with question marks) indicate the assumed approximate depth of the crust-mantle boundary beneath Central Java.

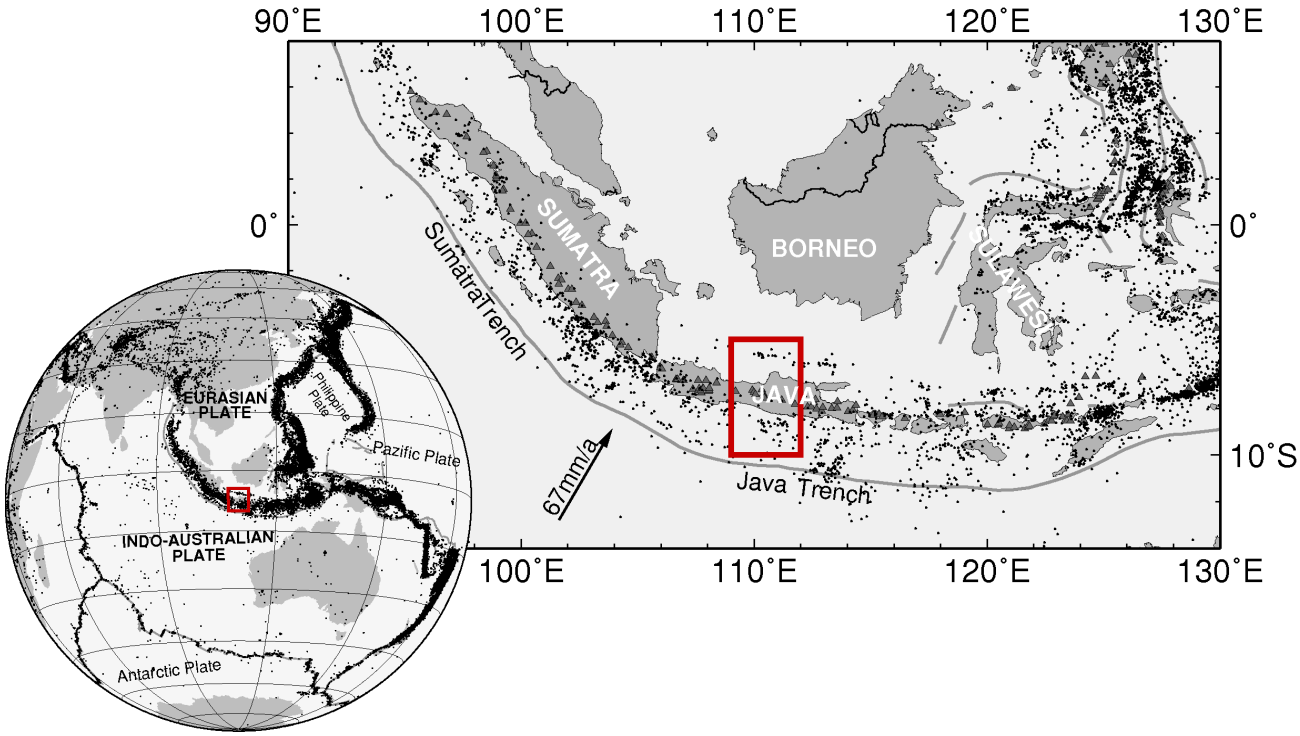
90˚E
100˚E
110˚E
120˚E
130˚E
0˚
10˚S
SUMATRA
BORNEO
SULAWESI
JAVA
Sumatra Trench
Java Trench
67mm/a
EURASIAN PLATE
Philippine Plate
Pazific Plate
INDO-AUSTRALIAN PLATE
Antarctic Plate

Figure 1

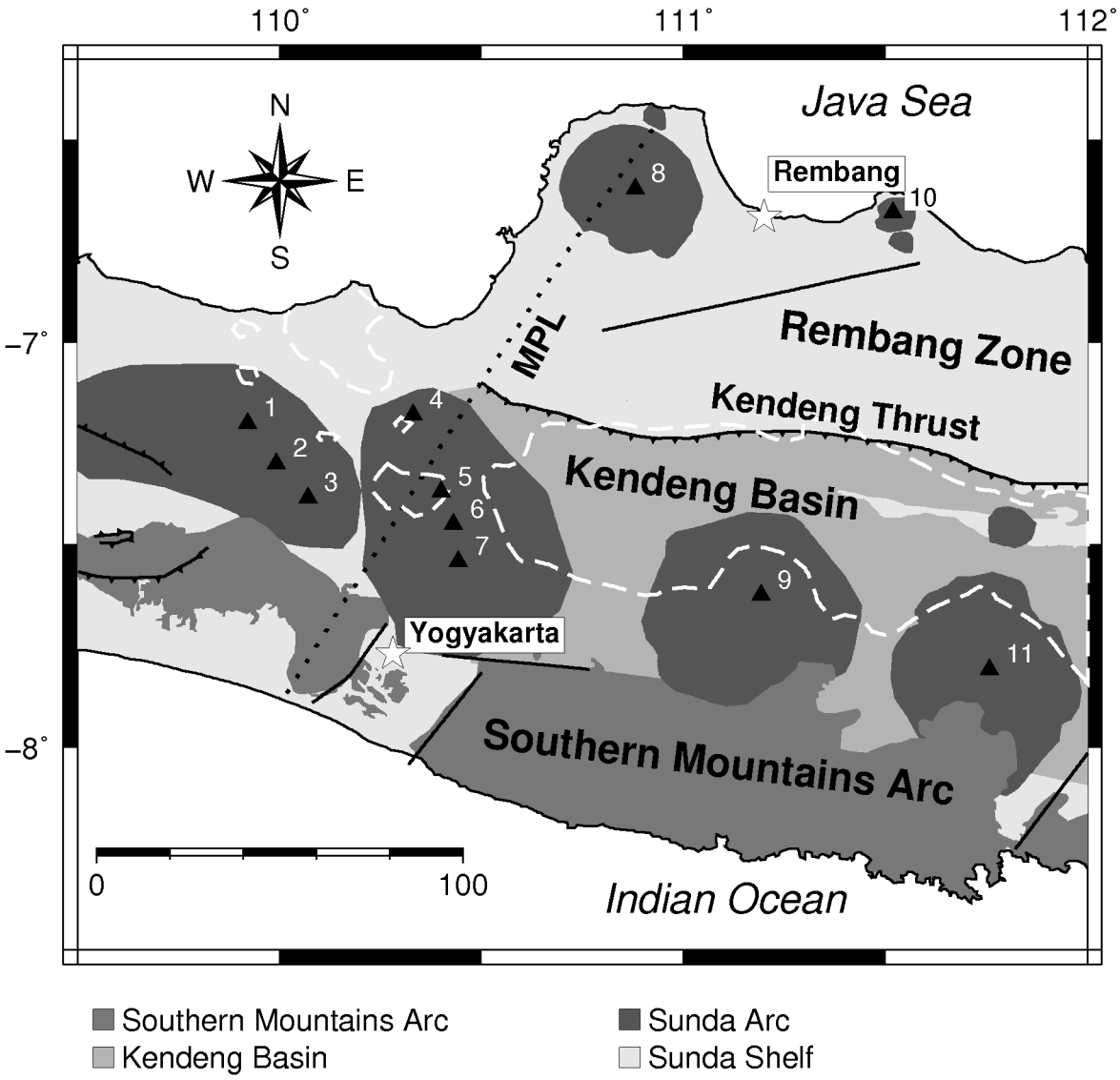
110˚
111˚
112˚
−7˚
−8˚
N
W
E
S
Java Sea
Rembang
MPL
Rembang Zone
Kendeng Thrust
Kendeng Basin
Yogyakarta
Southern Mountains Arc
Indian Ocean
0
100
1
2
3
4
5
6
7
8
9
10
11
Southern Mountains Arc
Kendeng Basin
Sunda Arc
Sunda Shelf

Figure 2

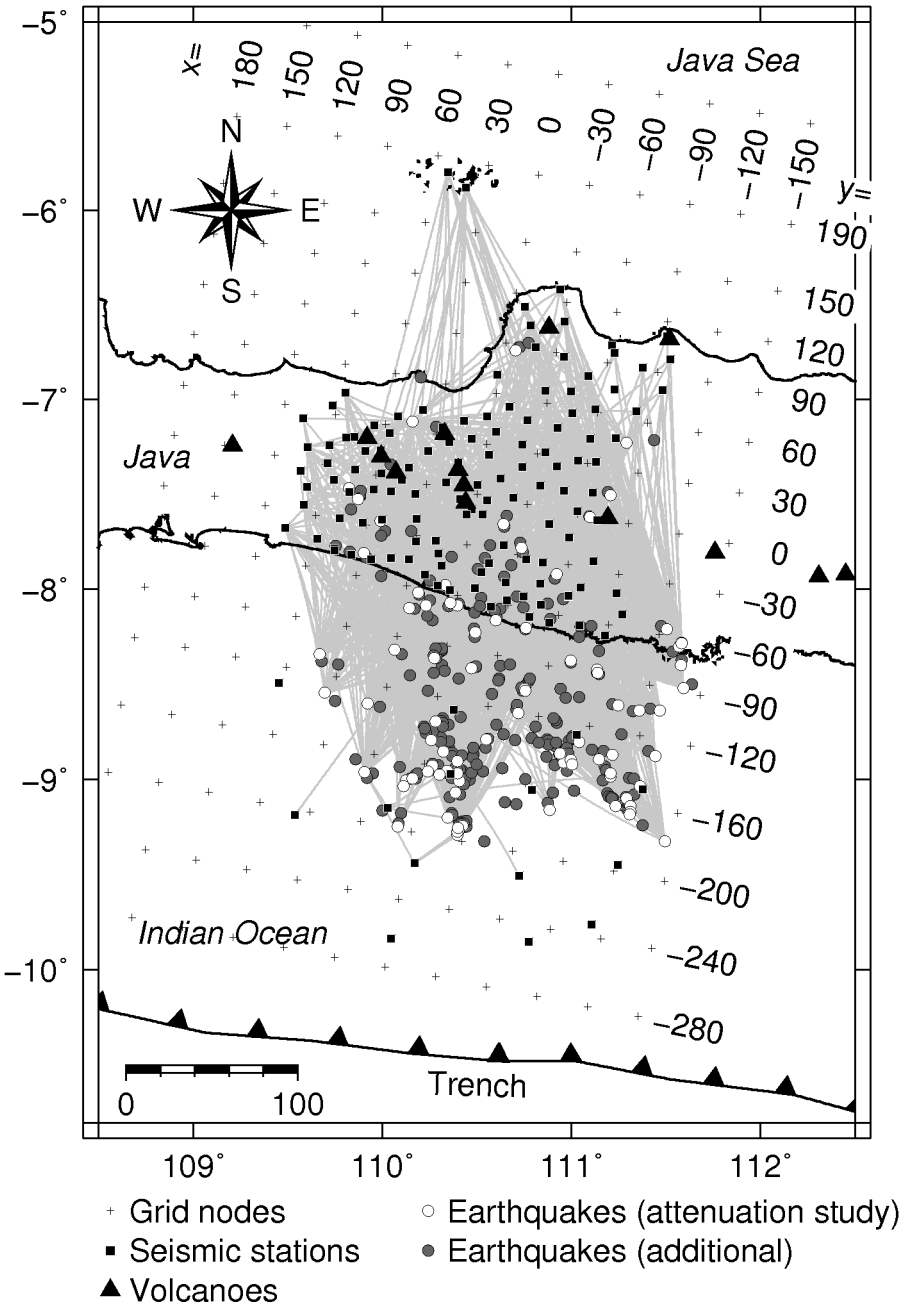
−5°
−6°
−7°
−8°
−9°
−10°
x=
180
150
120
90
60
30
0
−30
−60
−90
−120
−150
y=
190
150
120
90
60
30
0
−30
−60
−90
−120
−160
−200
−240
−280
N
W
E
S
Java Sea
Java
Indian Ocean
Trench
0
100
109°
110°
111°
112°
Grid nodes
Seismic stations
Volcanoes
Earthquakes (attenuation study)
Earthquakes (additional)

Figure 3

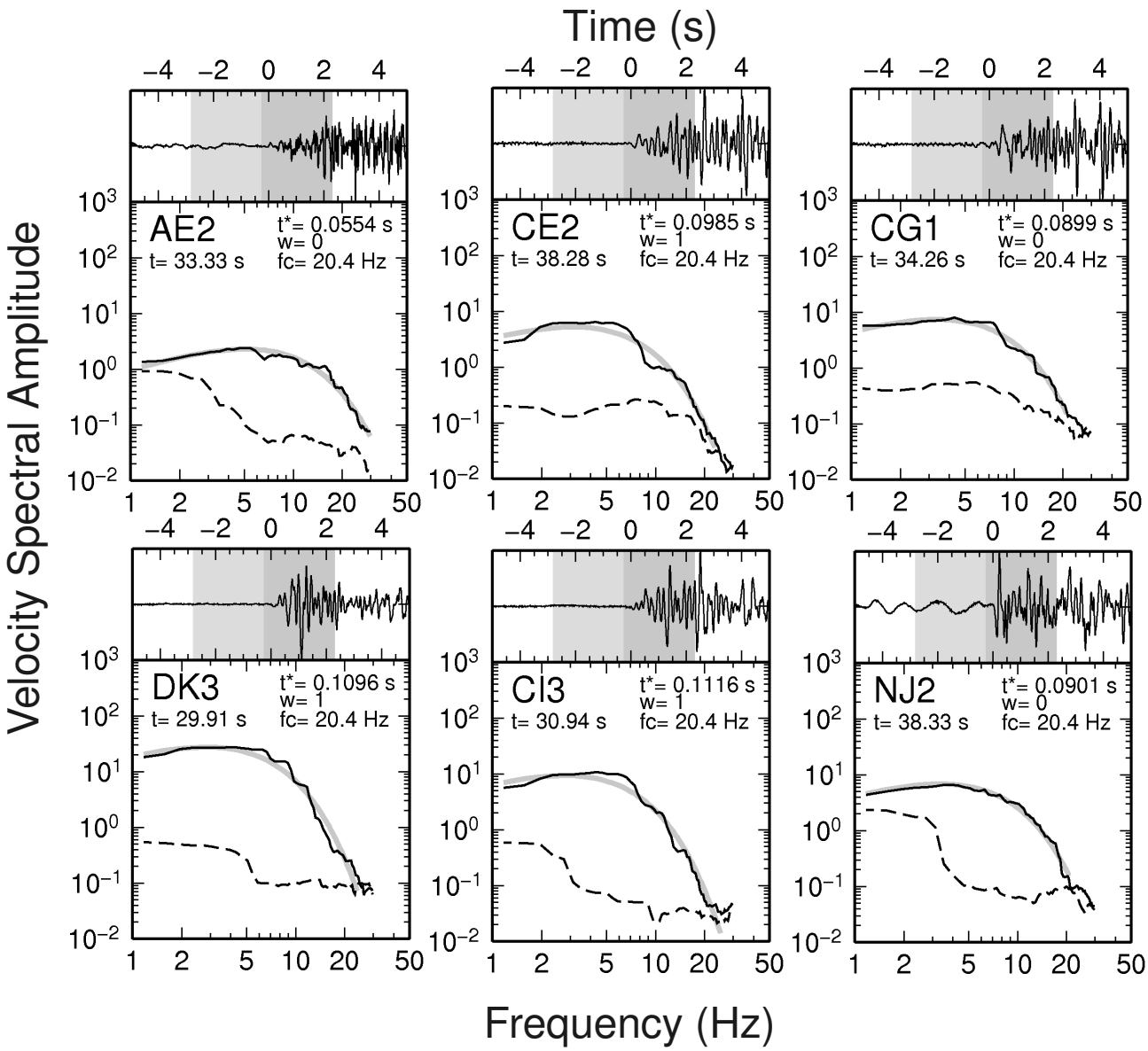
Time (s)
Velocity Spectral Amplitude
Frequency (Hz)
AE2
t*= 0.0554 s
w= 0
t= 33.33 s
fc= 20.4 Hz
CE2
t*= 0.0985 s
w= 1
t= 38.28 s
fc= 20.4 Hz
CG1
t*= 0.0899 s
w= 0
t= 34.26 s
fc= 20.4 Hz
DK3
t*= 0.1096 s
w= 1
t= 29.91 s
fc= 20.4 Hz
CI3
t*= 0.1116 s
w= 1
t= 30.94 s
fc= 20.4 Hz
NJ2
t*= 0.0901 s
w= 0
t= 38.33 s
fc= 20.4 Hz

Figure 4

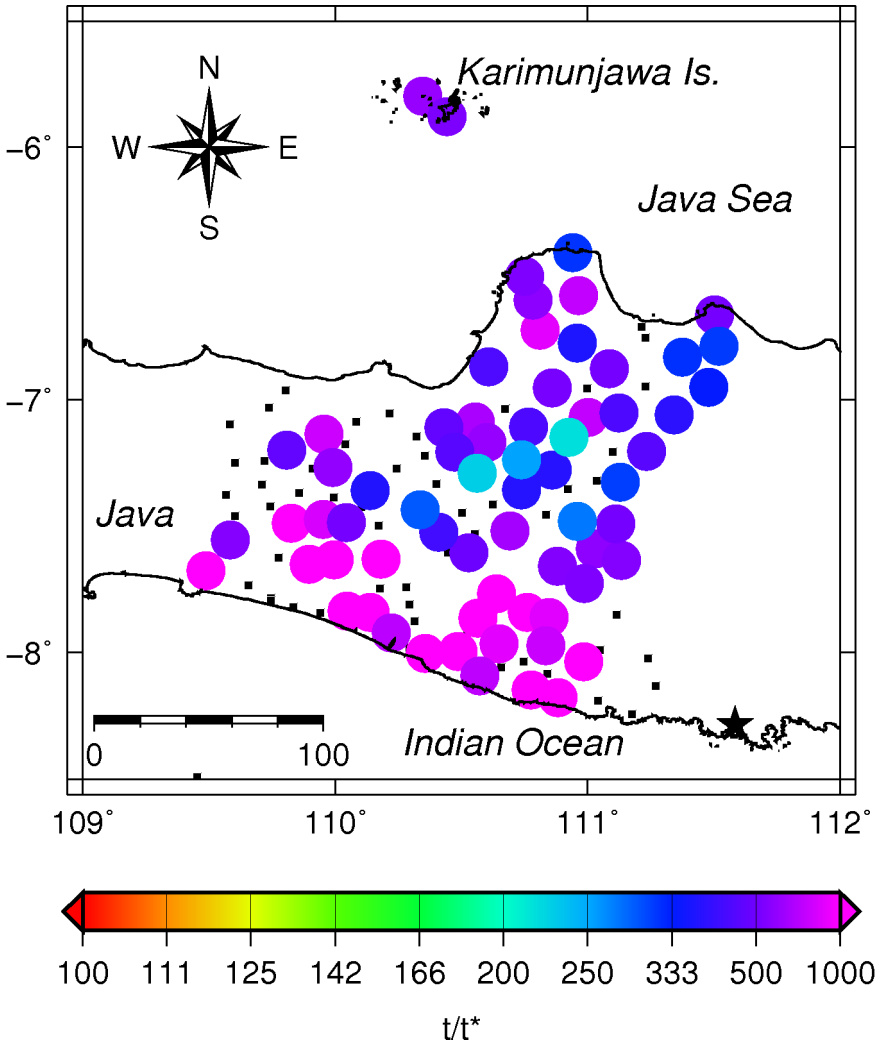
N
W
E
S
Karimunjawa Is.
Java Sea
Java
Indian Ocean
0
100
−6˚
−7˚
−8˚
109˚
110˚
111˚
112˚
100
111
125
142
166
200
250
333
500
1000
t/t*

Figure 5

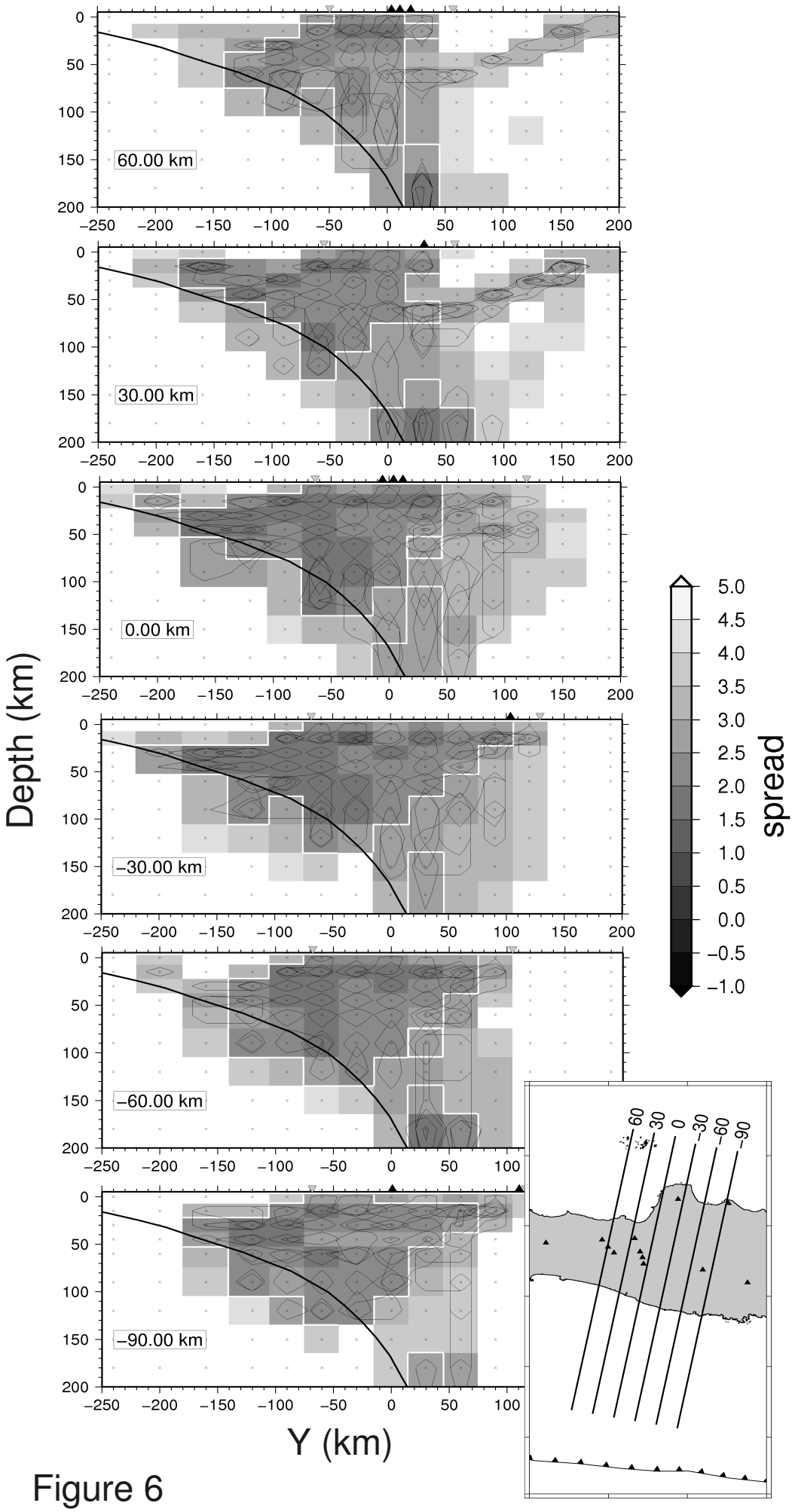
60.00 km
30.00 km
0.00 km
−30.00 km
−60.00 km
−90.00 km
Depth (km)
Y (km)
spread
5.0
4.5
4.0
3.5
3.0
2.5
2.0
1.5
1.0
0.5
0.0
−0.5
−1.0
60
30
0
−30
−60
−90

Figure 6

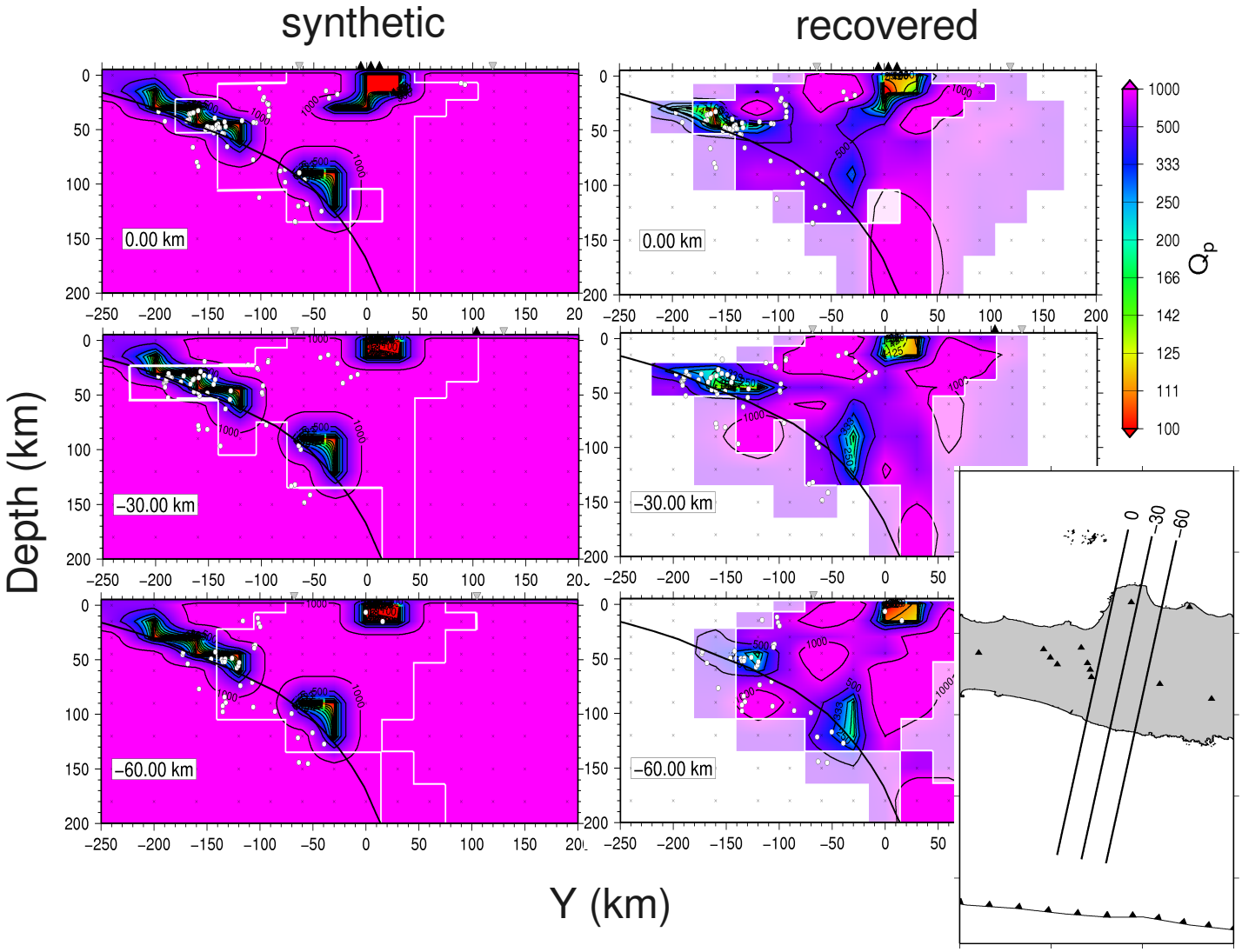
synthetic
recovered
Depth (km)
Y (km)
0.00 km
−30.00 km
−60.00 km
Qp
1000
500
333
250
200
166
142
125
111
100
0
−30
−60

Figure 7

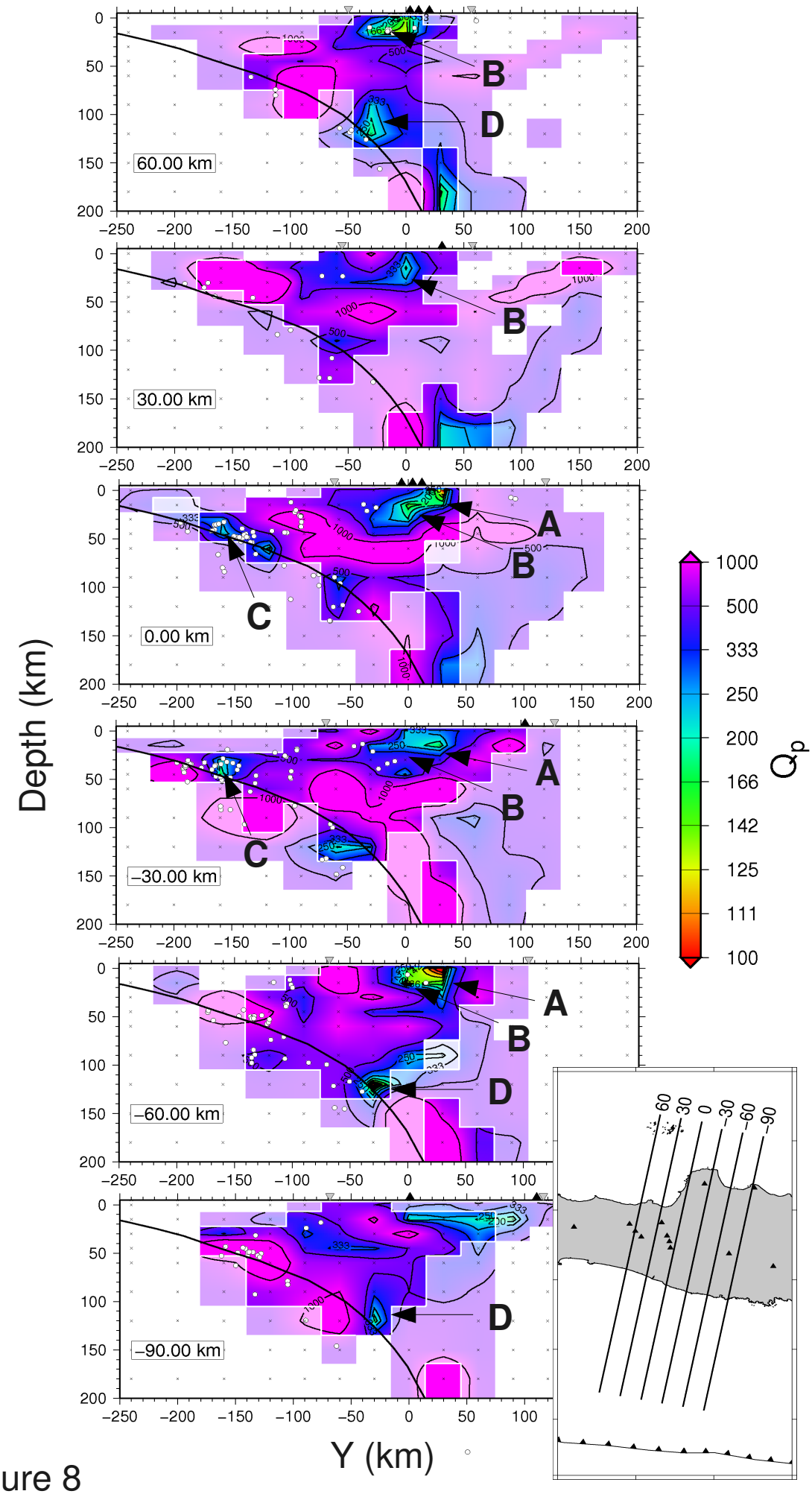
Depth (km)
Y (km)
60.00 km
30.00 km
0.00 km
−30.00 km
−60.00 km
−90.00 km
A
B
C
D
1000
500
333
250
200
166
142
125
111
100
Q_p
60
30
0
−30
−60
−90

Figure 8

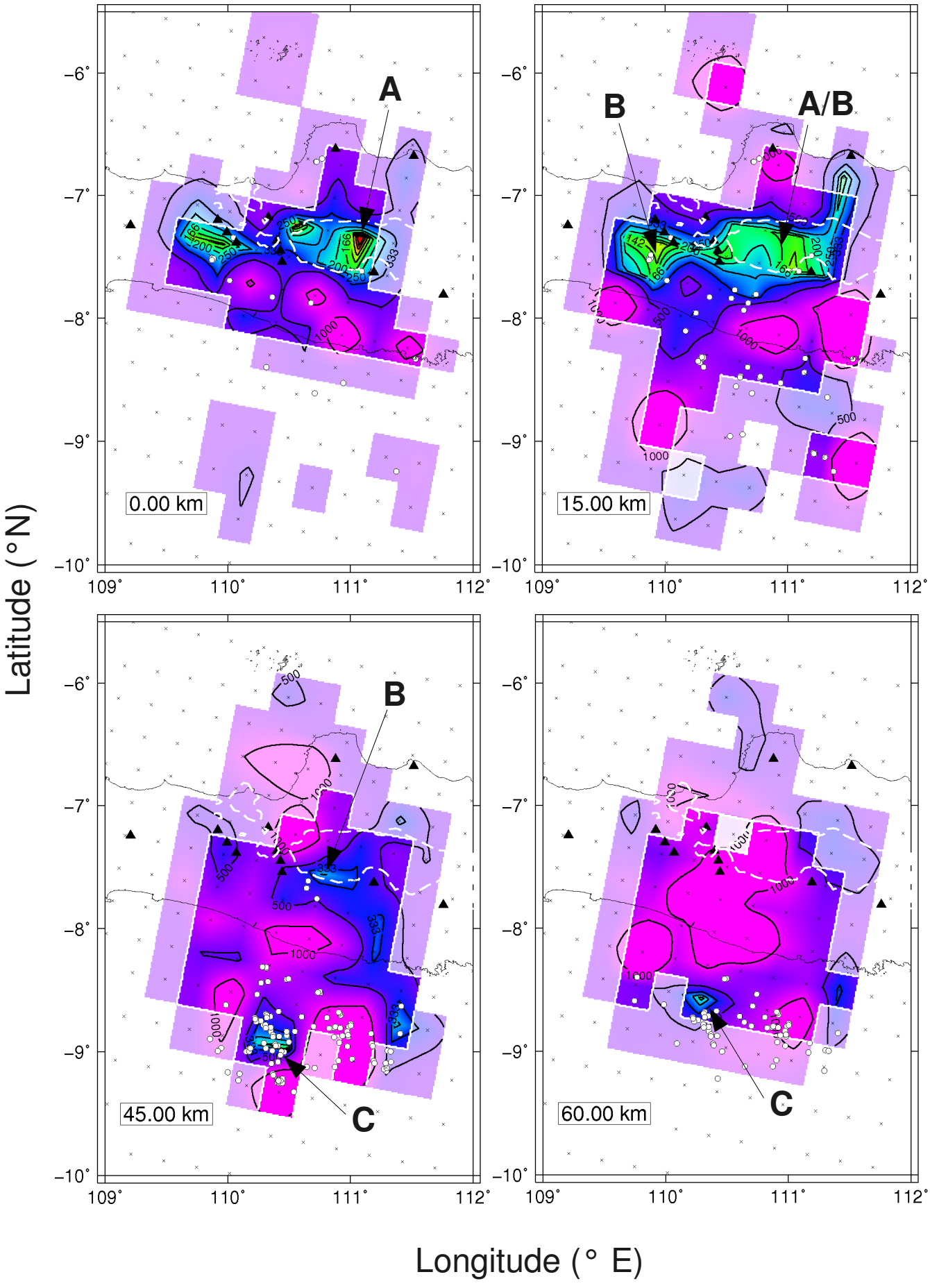
A
B
A/B
B
C
C
0.00 km
15.00 km
45.00 km
60.00 km
Latitude (° N)
Longitude (° E)
−6°
−7°
−8°
−9°
−10°
109°
110°
111°
112°

Figure 9

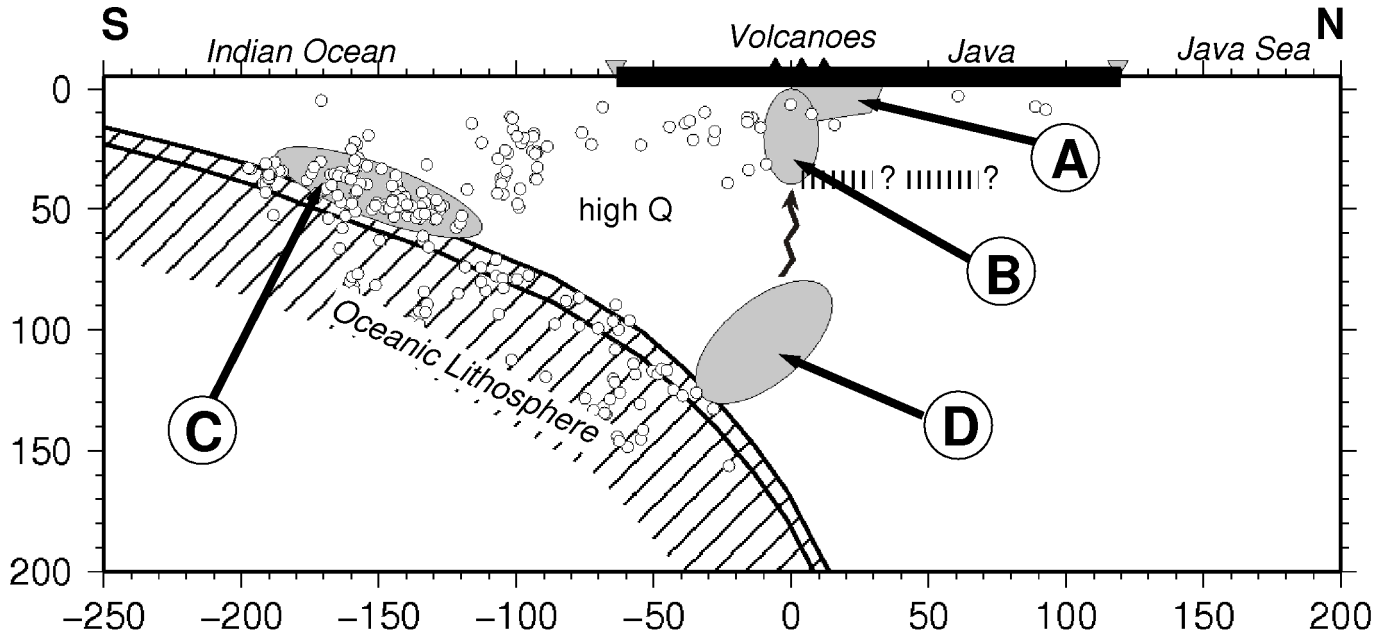
S
N
Indian Ocean
Volcanoes
Java
Java Sea
0
50
100
150
200
−250
−200
−150
−100
−50
0
50
100
150
200
high Q
? ? ?
A
B
C
D
Oceanic Lithosphere

Figure 10